

# Determining the morpho-kinematic properties of a face-on merger at $z \sim 0.7$

I. Fuentes-Carrera<sup>1,2</sup>, H. Flores<sup>1</sup>, Y. Yang<sup>1,3</sup>, S. Peirani<sup>4</sup>, F. Hammer<sup>1</sup>, M. Rodrigues<sup>1,5</sup>, and C. Balkowski<sup>1</sup>

<sup>1</sup> GEPI, Observatoire de Paris, UMR 8111 CNRS, Université Paris Diderot, 5 place Jules Janssen, 92190 Meudon, France

<sup>2</sup> Escuela Superior de Física y Matemáticas, Instituto Politécnico Nacional (ESFM-IPN), U.P. Adolfo López Mateos, edificio 9, Zacatenco, 07730 Mexico City, Mexico

e-mail: [isaura.fuentes@obspm.fr](mailto:isaura.fuentes@obspm.fr); [isaura@esfm.ipn.mx](mailto:isaura@esfm.ipn.mx)

<sup>3</sup> National Astronomical Observatories, Chinese Academy of Sciences, 20A Datun Road, Chaoyang District, Beijing 100012, PR China

<sup>4</sup> Institut d'Astrophysique de Paris, UMR 7095 CNRS, Université Pierre et Marie Curie, 98bis Bd Arago, 75014 Paris, France

<sup>5</sup> CENTRA, Instituto Superior Técnico, Av. Rovisco Pais 1049-001 Lisboa, Portugal

Received 18 August 2009 / Accepted 13 January 2010

## ABSTRACT

**Context.** At intermediate redshifts, many galaxies seem to have experienced an interaction. It is not always straightforward to determine what type of encounter or perturbation is observed, nor the outcome of this event. In some cases, only the use of both morphological and kinematical information can determine the true configuration of an encounter at intermediate redshift.

**Aims.** We present the morphological and kinematical analysis of a system at  $z = 0.74$  to understand its configuration, interacting stage, and evolution.

**Methods.** Using the integral field spectrograph GIRAFFE, long-slit spectroscopy by FORS2, direct optical images from the HST-ACS, and ISAAC near-infrared images, we determine the morphology of this system, its star-formation history, and its extended kinematics to propose a possible configuration for the system. Numerical simulations are used to test different interacting scenarios.

**Results.** We identify this system to be a face-on disk galaxy with a very bright bar that is interacting with a smaller companion such that the galaxy and the companion have a mass ratio of 3:1. The relevance of kinematical information and the constraints that it imposes on the interpretation of the observations of distant galaxies are particularly greater in this case.

**Conclusions.** This object represents one of the clearest examples of how one can misinterpret morphology in the absence of kinematical information.

**Key words.** galaxies: evolution – galaxies: interactions – galaxies: high-redshift – galaxies: kinematics and dynamics

## 1. Introduction

Understanding how and when galaxies formed is a fundamental question in astrophysics. To investigate galaxy evolution, one needs to understand how high-redshift galaxies evolve into the galaxies seen at low redshift. Galaxy formation and evolution in a cold dark matter (CDM) dominated universe can be described as follows. In the early universe, gas collapsed in dark matter halos, which later cooled to form stars, creating the first galaxies. These dark halos later merged to form larger dark halos and thus more massive galaxies (e.g., Cole et al. 2000; Somerville et al. 2001). In this hierarchical picture, galaxy interactions and mergers are an essential ingredient. Earlier numerical simulations demonstrated that disks form around previously existing spheroids by means of the smooth accretion of gas from the intergalactic medium (e.g., Steinmetz & Navarro 2002), whereas spheroids represent the remnants of major merger events where disks are thrown together and mixed violently on a short timescale (e.g., Toomre 1977; Barnes & Hernquist 1992; Mihos & Hernquist 1994). According to this scenario, disks are fragile: they are destroyed in major mergers and heated in minor mergers. However, simulations (Barnes 2002; Springel & Hernquist 2005) have also shown that gas-rich mergers can make new disks. These results support the spiral rebuilding scenario proposed by Hammer et al. (2005) in which mergers can also be responsible for the formation of disks. This

scenario renamed “disk survival” is also proposed by Hopkins et al. (2009).

We would like then to identify the types of merging episodes that end up as a disk galaxy. To do so, a joint analysis of morphological information with kinematical studies and spectral information is needed. The complementarity of these different types of analysis is essential to properly characterize distant galaxies to avoid any misinterpretations caused by the lack of resolution at higher redshifts. The IMAGES (Intermediate MAss Galaxy Evolution Sequence – Yang et al. 2008) program is an ESO Large Program exploiting data from large ground telescopes and from space for this purpose. IMAGES makes use of 1D and 2D spectroscopical data and direct imaging in the optical and the near-infrared (NIR) to shed more light on the following questions: How did galaxies form and assemble their stellar mass? When was the morphological differentiation between galaxies established? How did the Hubble Sequence form?

In this work, we present the morphological and kinematical analysis of J033227.07-274404.7, a system at  $z \sim 0.74$  displaying an unusually elongated, arc-like morphology with a velocity field that does not seem to match its observed morphology. Section 2 presents the overall properties of the object and the available data. In Sect. 3, the analysis of the data is presented, while in Sect. 4, we present the possible configuration of the system, as well as a numerical model of a probable encounter. Finally, in Sect. 5 we discuss the results and present the conclusions of this work.

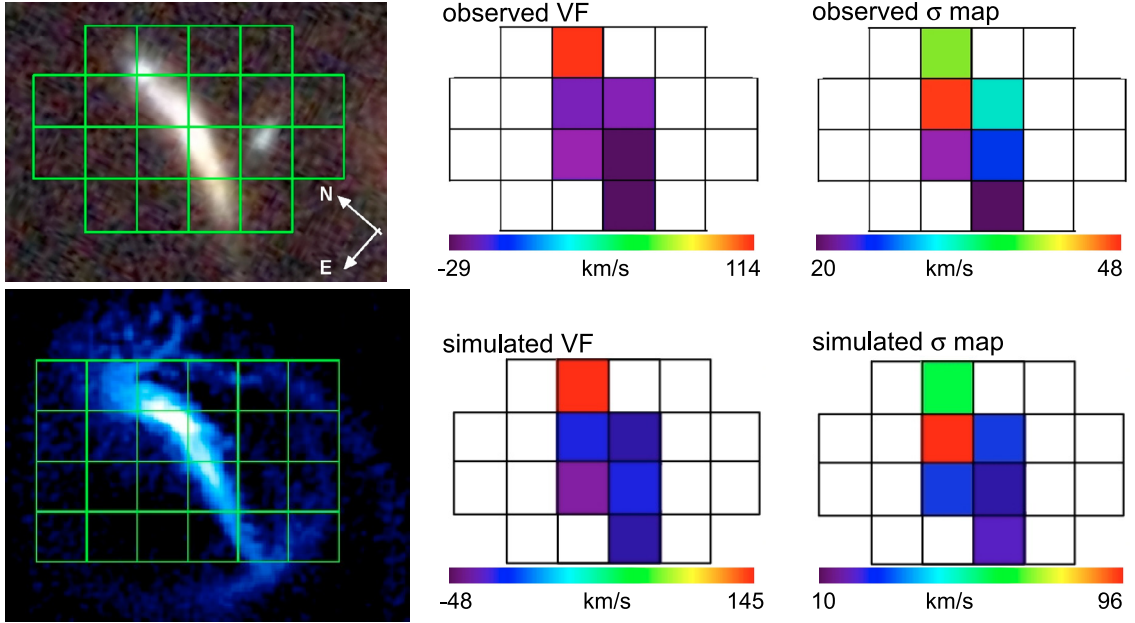


**Fig. 1.** *Top row, left panel:* composite image ( $B + V, i$  and  $z$  bands) of J033227.07-274404.7 taken with the Advanced Camera for Surveys (ACS) of the HST. Size of FoV is  $2.0 \text{ arcsec} \times 2.6 \text{ arcsec}$  ( $14.4 \text{ kpc} \times 18.8 \text{ kpc}$ ). Superimposed grid shows the position of the GIRAFFE IFU. *Top row, middle panel:* line-of-sight velocity map of the object derived from GIRAFFE observations of the  $[\text{OII}]3726,3729 \text{ \AA}$  doublet. *Top row, right panel:* velocity dispersion,  $\sigma$ , map of the object derived also from GIRAFFE observations. *Bottom row, left panel:* projected distribution of gas of the simulated encounter using the ZENO code (Barnes 2002). Snapshot shows the encounter just after the second peripassage (12 Myr after) and 1.93 Gyr after the first peripassage. The FLAMES IFU grid is superimposed to simulate the GIRAFFE observations. *Bottom row, middle panel:* line-of-sight velocity field derived from the ZENO simulation considering an IFU similar to that of GIRAFFE. *Bottom row, right panel:*  $\sigma$  map of the same simulation.

In this paper we adopt the following cosmological parameters:  $H_0 = 70 \text{ km s}^{-1} \text{ Mpc}^{-1}$ ,  $\Omega_M = 0.3$ , and  $\Omega_\Lambda = 0.7$ . Magnitudes are in the AB-system.

## 2. Data

J033227.07-274404.7 is an object in the Chandra Deep Field South (CDFs). High spatial resolution images of the system were taken from the HST archive. The images were obtained with the Advanced Camera for Surveys (ACS) in its Wide Field Channel (WFC) mode on the HST as part of the GOODS projects (Giavalisco et al. 2004). Images were taken in the following filters:  $F435W$ ,  $F606W$ ,  $F775W$ , and  $F850LP$  (Beckwith et al. 2006). These filters are close to the  $B$ ,  $V$ ,  $i$ , and  $z$  passbands, respectively. The publicly available version v1.0 of the reduced, calibrated, stacked, mosaicked, and drizzled images were used (drizzled pixel scale =  $0.03 \text{ arcsec}$ ). Ground-based images in the  $U$ ,  $B$ ,  $V$ ,  $R$ , and  $I$  bands were taken from the ESO Imaging Survey (EIS – Arnouts et al. 2001). These images were taken with the WFI camera on the MPG/ESO 2.2 m telescope. Each image has a pixel size of  $0.238 \text{ arcsec}$  with an average seeing of  $0.86 \text{ arcsec}$ . Images in the  $J$ ,  $H$ , and  $K_s$  bands were taken from the EIS deep survey (Vandame et al. 2001). These images were taken with ISAAC with a plate scale of  $0.15 \text{ arcsec/pix}$  with a reported seeing of  $0.6 \text{ arcsec}$ . The object is detected by Spitzer/IRAC in the mid-infrared (Dickinson et al., in preparation) and with Spitzer/MIPS in the far-infrared (Chary et al., in preparation). However, the object shows almost no emission at these wavelengths and is contaminated significantly by a southern galaxy at  $z > 1$ . The limiting magnitudes for these observations were 21.3 mag at  $24 \mu\text{m}$  for MIPS, and 26.15 mag, 25.66 mag, 23.79 mag, and 23.70 mag for IRAC’s channels one to four, respectively. The object was not detected by GALEX in

the FUV (probably because of the high redshift of the object). In the NUV, two sources are detected closer than  $2 \text{ arcsec}$  to the object. However, considering the pixel size of GALEX ( $1.5 \text{ arcsec}$ ), these detections might be contaminated by neighboring galaxies – especially the galaxy at  $z \sim 0.63$ . The object was not detected in CHANDRA observations down to  $5.5 \times 10^{17} \text{ ergs cm}^{-2} \text{ s}^{-1}$  in the  $0.5\text{--}2 \text{ keV}$  band and  $4.5 \times 10^{16} \text{ ergs cm}^{-2} \text{ s}^{-1}$  in the  $2\text{--}10 \text{ keV}$  band (Giacconi et al. 2002; Rosati et al. 2002).

For each image, photometry of the system was extracted within a constant aperture of  $3 \text{ arcsec}$  in diameter. Because of the large uncertainty associated with the zeropoint calibration of the  $H$ -band, we used the revised calibration proposed by Wuyts et al. (2008). Table 1 shows the photometry values and associated uncertainties for J033227.07-274404.7. Uncertainties in the extracted magnitudes correspond to the magnitude error given by SExtractor (Bertin & Arnouts 1996), and the systematic error associated with the uncertainty in the zeropoint (ZP) calibration. Because of the weakness of the emission for  $\lambda > 35.0 \mu\text{m}$  and the contamination by the galaxy at higher redshift, no photometry was extracted at these wavelengths.

Two-dimensional spectroscopic observations of J033227.07-274404.7 were taken with the integral field spectrograph FLAMES (Fibre Large Array Multi Element Spectrograph) with the medium-high ( $R = 5600\text{--}46000$ ) resolution spectrograph GIRAFFE (multi-IFU mode) as part of the IMAGES program (Yang et al. 2008). The object was observed with one IFU consisting of a rectangular array of 20 microlenses of  $0.52 \text{ arcsec}$  each, giving an aperture of  $2 \text{ arcsec} \times 3 \text{ arcsec}$ . The LR05 setup was used to observe the redshifted  $[\text{OII}]3726,3729 \text{ \AA}$  doublet. The line-of-sight velocity and velocity dispersion at each lenslet were derived following the procedure described in Flores et al. (2006).

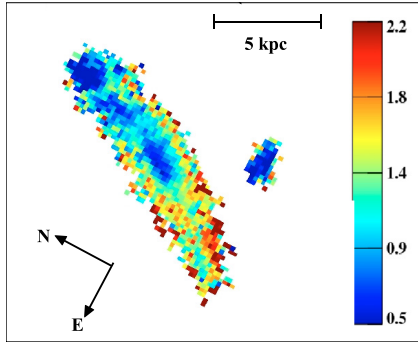


**Fig. 2.**  $(B - z)$  color image of J033227.07-274404.7 derived from the HST-ACS images.

A low-resolution ( $R = 860$ ), large wavelength-range long-slit spectrum (6000 Å to 10800 Å) of the object was taken with the visual and near UV Focal Reducer and low dispersion Spectrograph, FORS2 as part of the ESO-GOODS program of spectroscopy of faint galaxies in the CDFS (Vanzella et al. 2005). FORS2 was used in its multi-object spectroscopy with exchangeable masks (MXU) mode. The 300I grism was used to obtain a spectral resolution of 3.2 Å per pixel and a spatial scale plate of 0.126 arcsec/pix.

### 3. Analysis

#### 3.1. General properties

The top left panel of Fig. 1 shows the HST-ACS composite image of the object ( $F435W + F606W, F775W$  and  $850LP$  filters). The object displays an arc-like shape 2.04 arcsec long (14.3 kpc at the assumed redshift). The object seems to consist of an elongated structure about 1.52 arcsec (11.0 kpc) long and a smaller structure, 0.34 arcsec (2.45 kpc) long, located to the north-northwest of the main structure. The inner parts of the larger structure are brighter than the remaining structure and fainter, distorted emission is seen at each end of this elongated structure. Small discontinuities in the brightness of this structure are also seen. The smaller, northern, structure seems almost circular. A small faint structure is also seen to the southwest of the elongated structure.

Spectroscopic observations indicate that the object is at a redshift of 0.73814 with an uncertainty of 5 km s<sup>-1</sup> (Puech et al. 2008). It is surrounded by various objects. A disk-like galaxy to the southwest with a spectroscopic redshift of 1.128 and another galaxy-like object to the southeast with a photometric redshift of 0.63.

Figure 2 shows the  $(B - z)$  color image of the system. This bluest-minus-reddest band image shows that the northern part of the system is much bluer than the southern parts. The region corresponding to the northern smaller structure is the bluest one. Bluer colors are seen all the way from the center of the main galaxy to the companion. The smaller region to the southwest has very blue colors. It is important to notice however that in this image even the reddest colors correspond to a  $(B - z)$  value bluer than 2.7 mag. Following the analysis of Neichel et al. (2008), for a pure starburst region, the observed  $(B - z)$  of a galaxy at this redshift is bluer than 1.0 mag. A  $(B - z)$  value of 2.8 corresponds to a Sbc galaxy at the redshift of the object. So in general, the whole galaxy is forming stars, more importantly in the bluer regions. Dust has little influence on the color map since, as will be shown later (Sect. 3.3), attenuation is low.

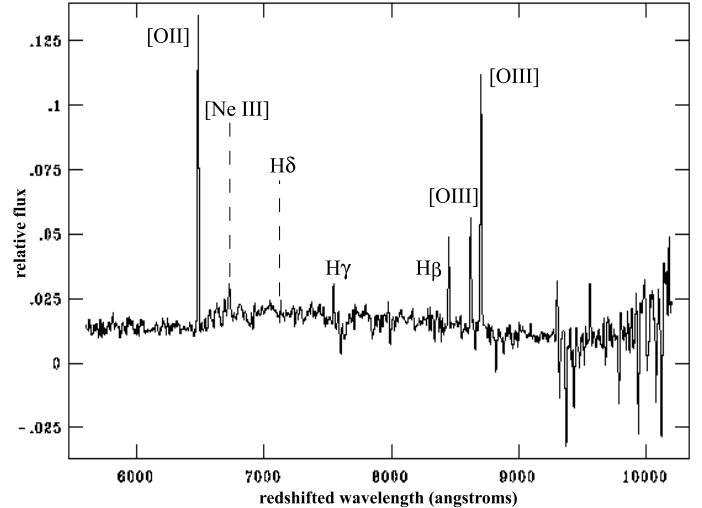


**Fig. 3.** FORS2 spectrum of J033227.07-274404.7 Redshifted wavelengths are shown. Relative flux is in energy per area unit per time unit per wavelength.

#### 3.2. Kinematics

Top middle panel of Fig. 1 shows the line-of-sight velocity field (VF) of the object. Only pixels with a signal-to-noise (S/N) value higher than 3 were taken into account when deriving the VF. The VF encompasses 2.33 arcsec ( $\sim 16.7$  kpc). Top left panel of Fig. 1 shows the superimposition of the IFU on the composite image of the system. The pixels corresponding to the elongated structure show a very uniform VF. For these pixels, the global velocity gradient is shallower than 14 km s<sup>-1</sup>. On the other hand, the upper northernmost pixel has a velocity that differs by more than 130 km s<sup>-1</sup> from that of the other pixels. The position of this pixel matches the location of the smaller, rounder structure to the north-northwest of the main structure. Top right panel of Fig. 1 shows the velocity dispersion ( $\sigma$ ) map of the object. Values of  $\sigma$  range from 20 km s<sup>-1</sup> to almost 50 km s<sup>-1</sup>. The pixel with the maximum value for the dispersion,  $\sigma = 48$  km s<sup>-1</sup>, corresponds to the region between the elongated structure and the smaller structure to the north-northwest. During the observation of this object, the median seeing was 0.805 arcsec. Considering the large size of each GIRAFFE spaxel (0.52 arcsec), the resulting velocity and dispersion velocity maps are not greatly affected by this value.

#### 3.3. Spectral energy distribution

The FORS2 spectrum of the system is shown in Fig. 3. The [OII]3726, 3729 Å doublet is easily identified, and H $\beta$ , H $\gamma$  and H $\delta$  are all seen in emission. The [OIII]4959, 5007 Å lines are also visible. We extracted some properties of the gas phase following the methodology described in Rodrigues et al. (2008). Since H $\gamma$ /H $\beta$  = 0.4, there is apparently no extinction. No evidence of AGN contamination was found and the  $\log[\text{OII}]/\beta = 0.55$  and  $\log[\text{OIII}]/\beta = 0.6$  ratios are concordant with the expected values of a HII region according to McCall et al. (1985). However, the [NeIII]3869 Å line is very strong and may be a signature of shocks. The metallicity of the gas is subsolar with  $12 + \log \text{O}/\text{H} = 8.48$  dex. This metallicity is typical of galaxies of mass  $\log M_* = 10.00$  dex at  $z \sim 0.7$  according to the stellar mass-gas phase metallicity relation (Rodrigues et al. 2008). To constrain the stellar population content of the

**Table 1.** Fluxes for J033227.07-274404.7 within 3.0 arcsec.

Filter	Magnitude $\pm$ error within 3 arcsec	Magnitude $\pm$ error main galaxy	Magnitude $\pm$ error companion
$U'_{\text{EIS}}$	$22.7826 \pm 0.0395$	—	—
$U_{\text{EIS}}$	$22.8260 \pm 0.0395$	—	—
$B_{\text{ACS}}$	$23.3267 \pm 0.0194$	$25.280 \pm 1.180$	$23.830 \pm 0.605$
$B_{\text{EIS}}$	$23.5340 \pm 0.0165$	—	—
$V_{\text{EIS}}$	$23.2758 \pm 0.0419$	—	—
$V_{\text{ACS}}$	$22.9400 \pm 0.0118$	$24.396 \pm 0.732$	$22.706 \pm 0.336$
$R_{\text{EIS}}$	$22.5642 \pm 0.0248$	—	—
$i_{\text{ACS}}$	$22.3859 \pm 0.0137$	$24.689 \pm 0.965$	$22.744 \pm 0.394$
$I_{\text{EIS}}$	$21.9494 \pm 0.0338$	—	—
$z_{\text{ACS}}$	$22.1979 \pm 0.0141$	$24.769 \pm 1.295$	$22.898 \pm 0.597$
$J_{\text{ISAAC}}$	$22.09 \pm 0.02$	—	—
$H_{\text{ISAAC}}$	$22.13 \pm 0.03$	—	—
$K_{\text{SISAAC}}$	$21.61 \pm 0.02$	—	—

**Notes.** <sup>a</sup> Last two columns show the extracted fluxes for the central parts of the main galaxy and the companion using POLYPHOT.

galaxy, we performed a fit to the observed spectrum with a linear combination of stellar libraries. We used a base of 39 template single-stellar-populations (SSPs) from Bruzual & Charlot (2007), of 13 ages (from 10 Myr to 5 Gyr) and 3 metallicities (subsolar, solar, and supersolar) using the STARLIGHT software (Cid-Fernandes et al. 2005). A Cardelli et al. (1989) extinction law was assumed. The best-fit relation indicates that a high fraction of the galaxy spectra is dominated by young stellar features typical of 13 Myr, 100 Myr, 200 Myr, and intermediate age stellar population of around 1 Gyr. However, the quality of the spectra, low S/N, and limited wavelength range does not allow us to provide strong constraints on the fractional contribution of light from stellar populations of different ages. To constrain the stellar population properties more reliably, we investigated the spectral energy distribution (SED) based on photometric measurements.

Figure 4 shows the SED of the entire system using the photometry values presented in Sect. 2. Wavelengths shown are rest-frame wavelengths. Flux is given in  $\text{erg/s/arcsec}^2/\text{angstrom}$ . For the optical part of the distribution, both the ACS-HST and EIS images were used. Full horizontal errorbars represent the FWHM of the photometric filters used in the corresponding surveys, while vertical errorbars represent the convolution of two terms: the magnitude error as given by SExtractor (Bertin & Arnouts 1996), and the systematic error associated with the uncertainty in the zeropoint calibration. The resulting SED shows a global decline from shorter to longer wavelengths. We adjusted a synthetic SED consisting of a linear combination of composite stellar populations (CSP) and a two parameter extinction law from Cardelli (1989). The base consists of 6 CSP from Charlot & Bruzual models (Charlot & Bruzual 2007) with a Salpeter IMF (Salpeter 1955) and a  $\tau$ -exponentially declining star formation history with  $\tau = 100$  Myr. According to the low metallicity detected in the gaseous phase, we selected CSP with sub-solar metallicity  $Z = 0.5 Z_{\odot}$ . The ages of the 6 stellar populations are 13 Myr, 200 Myr, 500 Myr, 1 Gyr, 4 Gyr, and 7 Gyr, respectively. The results for the bestfit relation ( $\chi^2 = 2.09$ ) are shown in Table 2. First two rows indicate the fraction of each CSP used for the fit. Last two rows show the fraction of stellar populations divided into young, intermediate, and old. We also present the median stellar-population mass fraction for solution in the 68% confidence interval. From the best fit, the stellar mass of the system is  $\log M = 10.00 \pm 0.35$  dex.

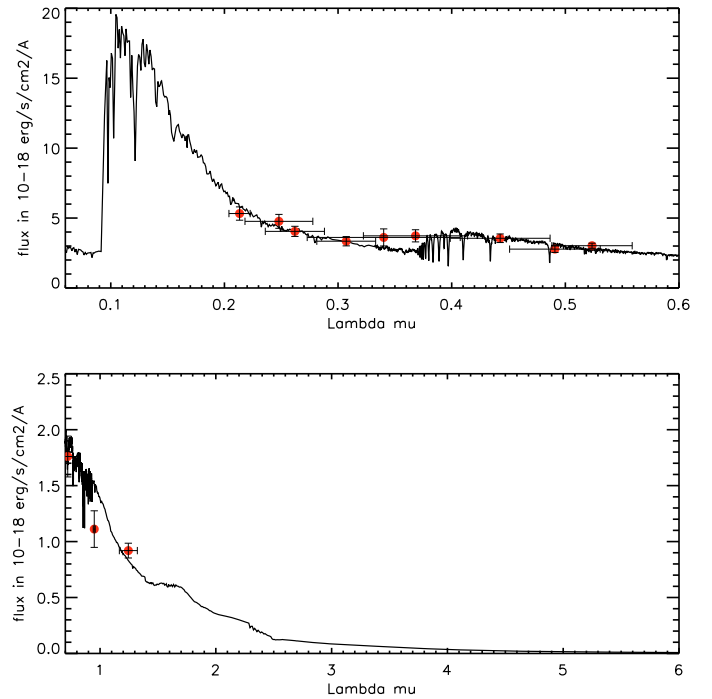


**Fig. 4.** *Top panel:* spectral energy distribution (SED) of J033227.07-274404.7 in the optical within a 3.0 arcsec aperture. *Bottom panel:* SED of J033227.07-274404.7 in the NIR. For both SEDs, the wavelengths shown are the rest-frame wavelengths. A SED compiled using stellar synthesis models by Bruzual & Charlot (2007) has been fitted to the object.

## 4. System configuration

### 4.1. Velocity field and sigma map vs. observed morphology

The composite image in the top left panel of Fig. 1 shows an elongated structure about 14 kpc long. Given the arc-like nature of the feature, the possibility that we observe a gravitational arc should be explored. Gravitational arcs were discovered more than twenty years ago (Soucail et al. 1987a). The origin of these structures is the gravitational lensing of light originating in a distant object by a dense mass distribution such as the core of

**Table 2.** Fraction of different stellar populations for the best fit to the SED of J033227.07-274404.7.

	Young (Myr)		Intermediate (Gyr)		Old (Gyr)	
	15	200	0.5	1	4	7
best fit	<0.01	0.16	0.08	0.05	0.05	0.65
median 68%	<0.01	0.15	0.22	0.07	–	0.55
best fit	0.17		0.13		0.70	
median 68%	$0.13 \pm 0.07$		$0.32 \pm 0.18$		$0.55 \pm 0.21$	

galaxy clusters (Hammer & Rigaut 1989; Estrada et al. 2007). To determine whether the structure seen is a gravitational arc, we analyzed the field of view (FoV) of J033227.07-274404.7 to search for any mass distribution at a given redshift that might be deflecting the light from a distant object (such as a cluster of galaxies). We used the GOODS catalog to search around a radius of  $180 \text{ arcsec}^1$  with a depth of  $25 \text{ mag/arcsec}^2$  and found at most two galaxies with a similar redshift ( $z \pm 0.3z$ ). This lack of galaxies with the same redshift can be interpreted as the absence of a particular mass distribution around the object (Soucail et al. 1987b), which excludes the possibility of a gravitational arc.

Once we exclude this possibility, we might suppose that the main, elongated structure is an inclined, distorted disk. If this were the case, the ellipticity of the main component of the system would equal  $\sim 0.76$ , giving an inclination angle of  $76 \text{ deg}$ , and implying that the disk is close to edge-on. Considering the extension of this disk ( $\sim 14 \text{ kpc}$  in diameter) and the mass derived from the SED fit, the disk should rotate with a velocity,  $V_{\text{rot}} \sim 80 \text{ km s}^{-1}$ , at  $7 \text{ kpc}$  from the center. Assuming the disk has an inclination of  $76 \text{ deg}$  and considering that the line-of-sight velocity,  $V_{\text{los}}$ , is given by  $V_{\text{los}} = V_{\text{rot}} \times \sin i$ , where  $i$  is the inclination of the system with respect to the plane of the sky, the gradient in the velocity field associated with the main structure of the system would be approximately  $80 \text{ km s}^{-1} \cdot 2$ .

However, the velocity field derived from GIRAFFE observations (top left panel of Fig. 1) shows a gradient smaller than  $15 \text{ km s}^{-1}$  within all the pixels associated with the main component of the system. A small gradient in the line-of-sight velocities in a disk galaxy is usually associated with an almost face-on system, where the contribution of the rotation velocity to the line-of-sight is small. In this case however, the morphology would seem to indicate that the system is almost edge-on in which case the line-of-sight velocity is similar to the rotation velocity of the system. So, which type of system are we actually observing?

The main clue is given by the VF. That there is almost no velocity gradient in the main component of the system can only be explained if the galaxy is seen face-on, in which case the bright, elongated structure seen in the direct images must be a bar lying on the disk of the main component. In this scenario, the disk would not be visible except for the faint structure seen to the southwest of the main galaxy. For bright barred galaxies in the Local Universe, the difference between the central magnitudes (in both the  $B$  and  $U$  bands) and the magnitudes of the outer parts of the disk can amount to  $5 \text{ mag/arcsec}^2$  (Kuchinski et al. 2000). The HST is only a  $2.5 \text{ m}$  telescope and the depth of the observation is an important issue for distant galaxies, whose emission is severely affected by cosmological dimming. For example, the optical radius (3.2 times the disk scale length) of a Milky-Way-like galaxy at  $z = 0.5$  requires  $3 \text{ h}$  of HST-ACS observations to be properly recovered, without accounting for extinction effects.

<sup>1</sup> At the distance of the object, this equals  $1.3 \text{ Mpc}$ .

<sup>2</sup> In this calculation, stellar mass of the entire system is being used, probably inferring a lower limit to  $V_{\text{rot}}$  and thus to  $V_{\text{los}}$ .

Considering that the observed magnitude of the central parts of the system is  $22.86 \text{ mag/arcsec}^2$  and that the GOODS detection limit is about  $25 \text{ mag/arcsec}^2$ , this diluted disk would not be detected in the direct HST-ACS images.

The formation of this bright bar could have been triggered by the interaction with a companion. This companion galaxy would be lying within the northernmost pixel of the IFU displaying emission. It would be orbiting around the main galaxy, moving with a velocity of at least  $130 \text{ km s}^{-1}$ . This velocity is estimated from the difference between the average velocity of the main galaxy ( $-22 \text{ km s}^{-1}$ ) and the velocity for the northernmost pixel (equal to  $114 \text{ km s}^{-1}$ ). This velocity difference would imply that the companion galaxy orbit lies outside the plane of the main galaxy. The velocity dispersion map of the system (top right panel of Fig. 1) shows a maximum of  $48 \text{ km s}^{-1}$  at the position between the companion and the northern tip of the main component, while the southern pixels associated with the main component show smaller values of velocity dispersion going from  $31.4 \text{ km s}^{-1}$  for the central parts of the galaxy to  $19.50 \text{ km s}^{-1}$  for the southern tip. The location of the maximum value of the velocity dispersion may correspond to the region in the system where the gas is most perturbed, indicating the interacting region between the main galaxy and the companion. If the small velocity gradient seen in the VF were the result of the superposition of several emission lines with different velocities for each IFU pixel (which would be the case if the galaxy had a large inclination value), then the velocity dispersion map would display much larger values (see Fig. 2 of Yang et al. 2008, for several examples regarding this situation). Also in favor of this interacting scenario is the blue feature in the color image of the system (Fig. 2) that could be enhanced star formation caused by a tidal perturbation and thus follow the passage of the northern companion. The strong [NeIII] lines seen in the FORS2 spectrum could be indicative of shocks produced by the interaction.

Assuming that there are two different interacting components, we estimated the mass ratio between them from their  $z$  band magnitudes. To do so, we extracted the photometry in the  $z$  band for each object. This was performed using the POLYPHOT task in IRAF<sup>3</sup>. Sky signal was computed as the average of the sky in four regions around the object. Considering the same mass-to-light ratio for both components, we find a mass ratio of 5 between the main component and the companion<sup>4</sup>.

#### 4.2. Numerical simulations of the encounter

To test the hypothesis of a face-on galaxy experiencing an encounter with a less massive galaxy, we performed several numerical simulations of plausible encounters using two different

<sup>3</sup> IRAF is distributed by the National Optical Astronomy Observatories, operated by the Association of Universities for Research in Astronomy, Inc., under cooperative agreement with the National Science Foundation.

<sup>4</sup> This value is actually a lower limit, since the companion is bluer than the main galaxy, as is shown in the color map (Fig. 2).

codes: ZENO developed by Barnes<sup>5</sup> (2002) and GADGET2 developed by Springel (2005). Both codes include standard N-body techniques for the collisionless components and smooth particle hydrodynamics (SPH) for the gaseous component.

In the ZENO simulations, the galaxy models are similar to those of Barnes (1998, 2002): a bulge with a shallow cusp (Hernquist 1990), an exponential disk of constant scale height (Freeman 1970; Spitzer 1942) and a dark matter halo with a constant density core (Dehnen 1993; Tremaine et al. 1994). The gas has the same properties as in Barnes (2002) and the SPH computation follows the isothermal equation of state. For the GADGET2 simulations, the galaxies are constructed using a spherical dark matter halo (with a Hernquist profile, Hernquist 1990), which contains a disk, consisting of stars and gas, and a bulge. Galaxies are created following Springel et al. (2005). Further details of the simulations using GADGET2 are given in Peirani et al. (2009). For the orbital parameters, several configurations were explored with both numerical codes: coplanar+direct, coplanar+retrograde, direct+slightly inclined orbits, and retrograde+slightly inclined orbit. All configurations followed parabolic orbits. Mass ratios of 3:1, 4:1, and 5:1 were tested.

The inclined and direct 3:1 mass ratio encounter as presented by Barnes (2002) seems to reproduce both the observed morphology and kinematics. For this particular simulation, the baryonic matter equals 20% of the dark matter. The gas is initially distributed identically to the disk component.

The total mass of the system (main galaxy and companion) was set to be 1.6666 mass units. In the ZENO code,  $G = 1$ . The length unit was set to be 95.3 kpc. Considering that the total stellar mass of the system derived from the SED fit equals  $10^{10} M_{\odot}$ , the other code units are  $1.41 \times 10^{11} M_{\odot}$  for the mass, 1.17 Gyrs for the time, and  $80 \text{ km s}^{-1}$  for the velocity. The simulation considered  $N_{\text{halo}} + N_{\text{stars}} + N_{\text{gas}} = 17856 + 21744 + 23994 = 63594$  particles. The progenitor disk in the model deviates from the Tully-Fisher relation (TF). When considering a disk that follows TF, the simulated bar is smaller than the observed one, although the global morphology of the feature, as well as the velocities derived, follow the observations.

To accurately compare the kinematics of the simulated encounter with the observed one, a grid resembling the GIRAFFE IFU was superimposed on the resulting snapshots. Velocities within each pixel of the grid were averaged to derive a velocity field similar to that shown in the top middle panel of Fig. 1. The middle panel of the bottom row in Fig. 1 shows a snapshot of the encounter at  $t = 1.65$  (1.93 Gyr) from the first peripassage and at  $t = 0.01$  (12.0 Myr) from the second one. The middle panel of the bottom row in the same figure shows the simulated velocity field of the gas, and the right panel of the same row shows the velocity dispersion map as it would be observed with the IFU of GIRAFFE. For both an inclined and retrograde 4:1 encounter and a 5:1 encounter, a thicker and rounder bar than the one seen in the observations is formed. In both of these cases, the velocity field trend is reproduced but the velocity dispersion peak is offset spatially relative to the observations. For this reason, the 3:1 encounter was chosen.

## 5. Discussion and conclusions

The simulated velocity field (bottom middle panel of Fig. 1) follows the same trend as the observed one (top middle panel

of the same figure), although the difference between the northernmost pixel and the average value of what seems to be the main galaxy, i.e., the other five pixels, is higher. For the observations, the difference is  $130 \text{ km s}^{-1}$ , while for the simulation the difference is  $169 \text{ km s}^{-1}$ . However, for the lower five pixels of the IFU, the velocity gradient of the simulation is also shallow. For the observations, the velocity gradient for these pixels equals  $14 \text{ km s}^{-1}$ , while for the simulations this gradient equals  $23 \text{ km s}^{-1}$ . For the velocity dispersion map, the distribution of the velocity dispersion in the simulated map (right bottom panel of Fig. 1) is similar to the observed one (top right panel of the same figure). The largest velocity dispersion value for the simulation is  $96 \text{ km s}^{-1}$ , while for the observations, this velocity dispersion peak has a value of  $48 \text{ km s}^{-1}$ . The average velocity dispersion value of the simulation ( $39 \text{ km s}^{-1}$ ) is close to that of the observations ( $31 \text{ km s}^{-1}$ ). Globally, the trends in both radial velocity and dispersion are followed. The observed morphology is also reproduced if cosmological dimming is taken into account. After scaling the particle density of the simulation to the observed magnitude of the central parts of the system ( $22.86 \text{ mag/arcsec}^2$ ), a difference of  $4 \text{ mag/arcsec}^2$  is clearly evident between the core of the system and the fainter structures of the underlying disk. Since the GOODS detection limit is about  $25 \text{ mag/arcsec}^2$ , the outer parts of the disk should not be detected in the direct images.

If we now follow the evolution of the simulation, a bar begins to form about 200 Myr after the first peripassage. This bar starts to fade before the second peripassage, but is enhanced once again when this second peripassage occurs. During the encounter, the disk is disrupted though not destroyed. To search for signs of a disrupted disk in our observations, we analyzed the raw FORS2 spectrum associated with the system searching for any particular features that could be related to the small feature seen southwest of the main galaxy. This small “blob” is hardly recognizable in the HST image in the top panel of Fig. 1, but can be seen in the color image in the bottom panel of the same figure. In the FORS2 spectra at the position of the main galaxy, a very slight asymmetry in the detected flux is seen. More flux seems to be detected on the side of the galaxy closer to the small “blob”. This may indicate that the “blob” has the same velocity as the main galaxy and thus belongs to its disk. Unfortunately, the resolution and S/N of the raw spectra do not allow us to draw a conclusive argument on this issue.

That the mass ratio from the measured light is lower than 3:1 can be explained by tidal stripping of the smaller galaxy during the direct encounter. The slight discontinuities seen in the brightness of the HST composite image may be caused by dust lanes. We note how these features seem to be transverse to the elongated structure. If this galaxy were edge-on, one would expect the dust lanes to appear along the main axis of the galaxy, that is along one side and the other of the bar. In contrast, these features appear to lie perpendicularly to this axis and may be related to arms or rings in the plane of the galaxy.

The simulation was allowed to evolve all the way to the post-merger stage. Figure 5 shows the evolution of the simulated encounter from the beginning of the encounter to the end of the merging process. The second snapshot in the top row shows the moment of the first peripassage. A zoom of the central parts of the system when the bar begins to form can be seen in the third snapshot of the top row of the figure. The second snapshot in the bottom row of the figure corresponds to the second peripassage of the galaxies, just 12 Myr before the observed morphology and kinematics of the system are reproduced. The rightmost snapshot in the bottom row of the figure shows the outcome of

<sup>5</sup> <http://www.ifa.hawaii.edu/~barnes/software.html>

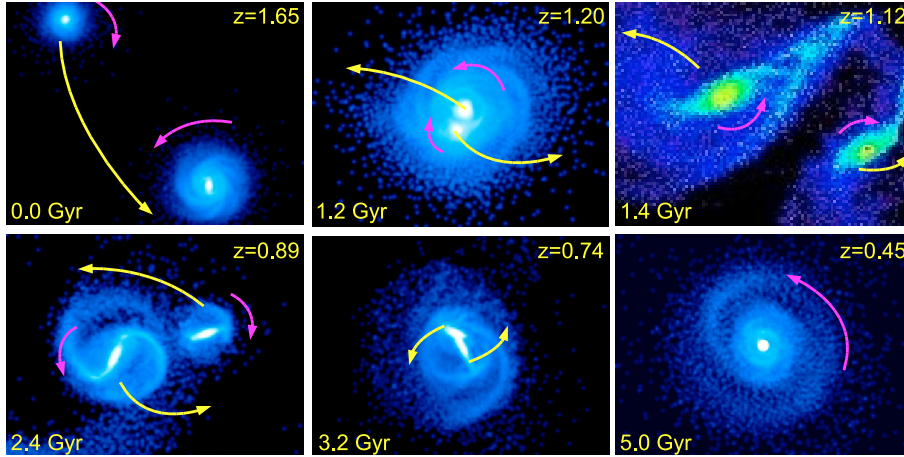


**Fig. 5.** From left to right, top to bottom: time evolution of the projected gas density of the simulated encounter from the beginning of the simulation until 5 Gyr after. The first peripassage of the galaxies, a zoom of the encounter at the moment when the bar begins to form, the time when galaxies are most distant after the first peripassage, and the second peripassage are shown. The size of frame differs for each snapshot to show different stages of the encounter. The fifth snapshot in the sequence shows the frame that is currently being “observed”.

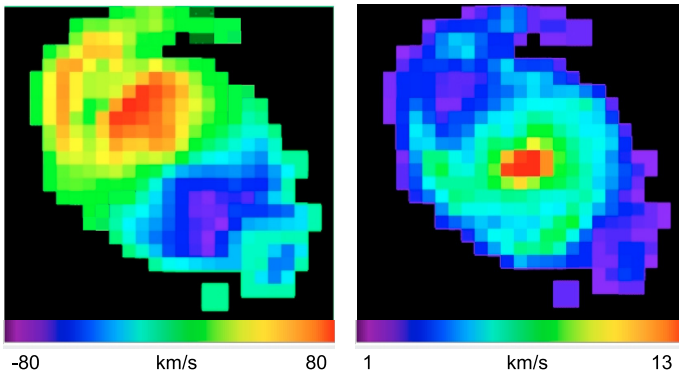


**Fig. 6.** *Left:* velocity field of the merger remnant 5 Gyr after the beginning of the simulation – last snapshot shown in Fig. 5. The velocity gradient associated with a slightly inclined rotating disk is clearly evident. *Right:* velocity dispersion map of the same snapshot. Maximum value coincides with the center of the merger remnant.

the merger. Figure 6 shows the VF and the velocity dispersion map computed for this snapshot. Resolution has been enhanced with respect to that of the GIRAFFE observations to be able to distinguish any particular velocity patterns. The VF derived for the merger remnant of the simulation shows a gradient similar to that of a slightly inclined rotating disk with an amplitude of  $\sim 160 \text{ km s}^{-1}$  from one end of the galaxy to the other. The velocity dispersion peak coincides with the center of this disk as expected for a rotating disk.

Thus the product of this 3:1 merger appears to be a disk galaxy. For this simulation, we note that the fraction of gas considered at the beginning of the simulation equals 12% of the mass of the disk, which is the gas fraction also used by Barnes in his simulations of the mergers of gas-rich disk galaxies (Barnes 2002). For the observed system, the gas fraction of the progenitor is much higher. This fraction can be computed following the method by Hammer et al. (2009a) which takes into account the SED fit, the SFR of the system, and the merger dynamical time (see Hammer et al. 2009a,b; and Puech et al. (2009) for further details). Following this computation, the initial fraction of gas in the progenitor amounts to 60% of the disk mass. Hopkins et al. (2009) demonstrated that if the gas fraction of the progenitor galaxy is 60–80% of the disk mass, the disk will be rebuilt after

an encounter, even if the mass ratio is 1:1. So in the case of this system, for which the gas fraction is high and the mass ratio is 3:1, a disk is the expected outcome of the merging process. This can be seen from the simulations even if the gas fraction considered for the simulated progenitor is considerably lower. In this case, the mass ratio and the configuration of the encounter are such that a disk is formed even if the gas fraction is relatively low, as the simulations have shown.

We have presented results from multiwavelength observations of J033227.07-274404.7, a perturbed system at  $z = 0.74$ . Using various techniques, we have analysed the morphology, star-formation history, and kinematics of this elongated, arc-like system. The analysis of the surroundings of this system have excluded the possibility of a gravitational arc. Although the morphology may be indicative of an almost edge-on galaxy, the kinematical data places very important constraints, which have led us to explore other possible configurations. This system seems to be composed of an almost face-on disk galaxy and a second disk galaxy 3 times less massive following an inclined orbit. The presence of a rather young stellar population on both components suggests ongoing enhanced star-formation caused by the interacting process. Numerical simulations have been used to trace the history of the encounter. We appear to be witnessing the encounter at its second passage. The analysis of this system indicates the necessity of combining both morphology, photometry, kinematics, and numerical simulations to disentangle the complex systems seen at intermediate redshifts and to determine the outcome of their evolution. This object is amongst the most striking examples of how one may misinterpret morphology in the absence of sufficient kinematical information.

*Acknowledgements.* I.F.C. acknowledges the Sixth Program of the EU for a Marie Curie Fellowship, as well as the H.H. FC Foundation for their financial and moral support.

## References

- Abraham, R. G., Tanvir, N. R., Santiago, B. X., et al. 1996, MNRAS, 279, 47
- Arnouts, S., Vandame, B., Benoist, C., et al. 2001, A&A, 379, 740
- Barnes, J. E. 1988, ApJ, 331, 699
- Barnes, J. E. 1998, in Galaxies: Interactions and Induced Star Formation, ed. R. C. Kennicutt, Jr. F. Schweizer, J. E. Barnes, D. Friedli, L. Martinet, & D. Pfenniger (Berlin, Springer-Verlag), 275

- Barnes, J. E. 2002, *MNRAS*, 333, 481
- Barnes, J. E., & Hernquist, L. E. 1992, *ARA&A*, 30, 705
- Beckwith, S. V. W., Stiavelli, M., & Koekemoer, A. M. 2006, *AJ*, 132, 1729
- Bell, E. F., McIntosh, D. H., Katz, N., & Weinberg, M. D. 2003, *ApJS*, 149, 289
- Bershady, M. A., Verheijen, M. A. W., & Crawford, S. M. 2008, *The Evolution of Galaxies through the Neutral Hydrogen Window*, ed. Minchin, R., & Momjian, E., to appear (AIPCS), in press [arXiv:0805.1743v1]
- Bertin, E., & Arnouts, S., 1996, *A&AS*, 117, 393
- Bouwens, R. J., & Illingworth, G. D. 2006, *Nature*, 443, 189
- Brinchmann, J., Abraham, R. G., Schade, D., et al. 1998, *ApJ*, 499, 112
- Bruzual, G. 2007, *From stars to galaxies: building the pieces to build up the Universe*, ASP Conf. Ser., ed. A. Vallenari, R. Tantaló, L. Portinari, & A. Moretti, [arXiv:astro-ph/0702091]
- Bruzual, G., & Charlot, S. 2003, *MNRAS*, 244, 1000
- Cardelli, J. A., Clayton, G. C., & Mathis, J. S. 1989, *ApJ*, 345, 245
- Carlberg, R. G., Cohen, J. G., Patton, D. R., et al. 2000, *ApJ*, 532, L1
- Chabrier, G. 2003, *PASP*, 115, 763
- Cid Fernandes, R., Mateus, A., Sodré, L., Stasinska, G., & Gomes, J. M. 2005, *MNRAS*, 358, 363
- Cole, S., Lacey, C. G., Baugh, C. M., & Frenk, C. S. 2000, *MNRAS*, 319, 168
- Combes, F. 2005, *AIP Conf. Proc.*, 783, 43
- D'Odorico, S. 1990, *The Messenger*, 61, 51
- Dehnen, W. 1993, *MNRAS*, 265, 250
- Estrada, J., Annis, J., Diehl, H. T., et al. 2007, *ApJ*, 660, 1176
- Flores, H., Hammer, F., Thuan, T. X., et al. 1999, *ApJ*, 517, 148
- Flores, H., Hammer, F., Puech, M., Amram, P., & Balkowski, C. 2006, *A&A*, 455, 107
- Freeman, K. C. 1970, *ApJ*, 160, 811
- Giacconi, R., Zirm, A., Wang, J., et al. 2002, *ApJS*, 139, 369
- Giavalisco, M., Ferguson, H. C., Koekemoer, A. M., et al. 2004, *ApJ*, 600, 93
- Hammer, F., & Rigaut, F. 1989, *A&A*, 226, 45
- Hammer, F., Flores, H., Elbaz, D., et al. 2005, *A&A*, 430, 115
- Hammer, F., Flores, H., Yang, Y., et al. 2009a, *A&A*, 496, 381
- Hammer, F., Flores, H., Puech, M., et al. 2009b, *A&A*, 507, 1313
- Heavens, A., Panter, B., Jimenez, R., & Dunlop, J. 2004, *Nature*, 428, 625
- Hernquist, L. 1990, *ApJ*, 356, 359
- Hopkins, P. F., Cox, T. J., Younger, J. D., & Hernquist, L. 2009, *ApJ*, 691, 1168
- Khochfar, S., & Burkert, A. 2006, *A&A*, 445, 403
- Kuchinski, L. E., Freedman, W. L., Madore, B. F., et al. 2000, *ApJS*, 131, 441
- Le Floch, E., Papovich, C., Dole, H., et al. 2005, *ApJ*, 632, 169
- Lotz, J. M., Davis, M., Faber, S. M., et al. 2007, *ApJ*, 672, 177
- Madau, P., Ferguson, H. C., Dickinson, M. E., et al. 1996, *MNRAS*, 283, 1388
- McCall, M. L., Rybski, P. M., & Shields, G. A. 1985, *ApJS*, 57, 1
- Mihos, J. C., & Hernquist, L. 1994, *ApJ*, 437, L47
- Neichel, B., Hammer, B., Puech, M., et al. 2008, *A&A*, 484, 159
- Neuschaefer, L. F., Im, M., Ratnatunga, K. U., Griffiths, R. E., & Casertano, S. 1997, *ApJ*, 480, 59
- Peirani, S., Hammer, F., Flores, H., Yang, Y., & Athanassoula, E. 2009, *A&A*, 496, 51
- Puech, M., Flores, H., Hammer, F., et al. 2008, *A&A*, 484, 173
- Puech, M., Hammer, F., Flores, H., et al. 2009, *A&A*, 493, 899
- Ravikumar, C. D., Puech, M., Flores, H., et al. 2007, *A&A*, 465, 1099
- Renzini, A., & da Costa, L. N. 1997, *The Messenger*, 87, 23
- Rodrigues, M., Hammer, F., Flores, H., et al. 2008, *A&A*, 492, 371
- Rosati, P., Tozzi, P., Giacconi, R., et al. 2002, *ApJ*, 566, 667
- Salpeter, E. E. 1955, *ApJ*, 121, 161
- Santos, J. F. C. Jr., Alloin, D., Bica, E., & Bonatto, C. J. 2002, in *Extragalactic Star Clusters*, IAUS, 207, 727
- Schimnovich, D., Ilbert, O., Arnouts, S., et al. 2005, *ApJ*, 619, L47
- Somerville, R. S., Primack, J. R., & Faber, S. M. 2001, *MNRAS*, 320, 504
- Soucail, G., Fort, B., Mellier, Y., & Picat, J. P. 1987a, *A&A*, 172, L14
- Soucail, G., Mellier, Y., Fort, B., Hammer, F., & Mathez, G. 1987b, *A&A*, 184, L7
- Springel, V. 2005, *MNRAS*, 364, 1105
- Springel, V., & Hernquist, L. 2005, *ApJ*, 622, L9
- Steinmetz, M., & Navarro, J. F. 2002, *NewA*, 7, 155
- Tremaine, S., Richstone, D. O., Byun, Y.-I., et al. 1994, *AJ*, 107, 634
- van den Bergh, S., Cohen, J. G., Hogg, D. W., & Blandford, R. 2000, *AJ*, 120, 2190
- Vanzella, E., Cristiani, S., Dickinson, M., et al. 2006, *A&A*, 434, 53
- Wuyts, S., Labbé, I., Förster Schreiber, N. M., et al. 2008, *ApJ*, 682, 985
- Yang, Y., Flores, H., Hammer, F., et al. 2008, *A&A*, 477, 789